The International Journal of Advanced Manufacturing Technology (2019) 105:4071–4084
https://doi.org/10.1007/s00170-018-2367-1

ORIGINAL ARTICLE

Research on the collaborative machining method for dual-robot mirror milling

Ju-Liang Xiao[1] · Su-Lei Zhao[1] · Hao Guo[1] · Tian Huang[1] · Bin Lin[1]

Received: 15 January 2018 / Accepted: 18 June 2018 / Published online: 30 June 2018

Abstract

To achieve the green and efficient processing of weak rigid large thin-walled aerospace parts, mirror milling systems are replacing traditional processing methods. A novel dual-robot mirror milling system consisting of a machining hybrid robot, supporting hybrid robot, and fixture is presented in this study. The cutter and the flexible supporting head are installed at the end of the machining robot and the supporting robot respectively. Because the deformation and vibration of the workpiece are directly affected by the collaborative performance of the cutter and the supporting head, the key problem is how to achieve collaborative machining by the cutter and the flexible supporting head in equal wall thickness machining. A collaborative machining method is proposed by establishing a relative pose relationship between the cutter and the supporting head. In this method, the cutter trajectory of the machining robot is generated in real time according to the end trajectory of the off-line planning supporting robot and the preset machining parameters. Next, the control parameters of each driving motor are obtained by the kinematics for the machining robot. A dual-robot endmost geometrical pose is used to obtain the machining wall thickness via contact-type online measurement for replacing ultrasonic thickness measurement systems. The wall thickness error is compensated by the machining robot for accurately controlling the machining thickness. Finally, a triangular grid is machined to verify the effectiveness of the proposed machining method in the proposed mirror milling system.

Keywords Mirror milling · Collaborative machining · Dual robots · Equal wall thickness · Large thin-walled parts

Electronic supplementary material The online version of this article (https://doi.org/10.1007/s00170-018-2367-1) contains supplementary material, which is available to authorized users.

✉ Ju-Liang Xiao
tjxjl@tju.edu.cn

Su-Lei Zhao
zhaosulei@tju.edu.cn

Hao Guo
guohaohalo@163.com

Tian Huang
tianhuang@tju.edu.cn

Bin Lin
tdlinbin@126.com

[1] Key Laboratory of Mechanism Theory and Equipment Design of State Ministry of Education, Tianjin University, Tianjin 300350, China

Nomenclature

$B-xyz$	Base coordinate system
$P-x_py_pz_p$	The coordinate system of the fixed moving platform
$C-x_cy_cz_c$	Terminal coordinate system of robot
$\boldsymbol{s}_1$, $\boldsymbol{s}_2$, $\boldsymbol{s}_3$	Unit vectors of coordinate system $P-x_py_pz_p$
u, $\boldsymbol{v}$, $\boldsymbol{w}$	Unit vectors of coordinate system $C-x_cy_cz_c$
q_i	Length of the rod in UPS branch i
$\boldsymbol{w}_i$	Unit vector of UPS branch i
d_v	Coordinate of $\boldsymbol{v}$ in coordinate system $C-x_cy_cz_c$
d_w	Coordinate of $\boldsymbol{w}$ in coordinate system $C-x_cy_cz_c$
x, y, z, α, β	Parameters of the position and orientation of TriMule
q_1, q_2, q_3, θ_1, θ_2	Lengths and angles of each branch of TriMule

$B_1{-}x_{B_1}y_{B_1}z_{B_1}$	Base coordinate system of the supporting robot
$C_1{-}x_{C_1}y_{C_1}z_{C_1}$	Tool coordinate system of the supporting robot
$S-x_Sy_Sz_S$	Followed coordinate system of the supporting head
$C_y{-}x_{C_y}y_{C_y}z_{C_y}$	Supporting cylinder coordinate system
$B_2{-}x_{B_2}y_{B_2}z_{B_2}$	Base coordinate system of the machining robot
$C_2{-}x_{C_2}y_{C_2}z_{C_2}$	Tool coordinate system of the machining robot
$T-x_Ty_Tz_T$	Followed coordinate system of the cutter
$V-x_Vy_Vz_V$	Virtual coordinate system of the cutter
$W-x_Wy_Wz_W$	Workpiece coordinate system
x_i, y_i, z_i, α_i, β_i	Parameters of the ith supporting robot pose in $W-x_Wy_Wz_W$
x_{si}, y_{si}, z_{si}, α_{si}, β_{si}	Parameters of the$i$th supporting robot pose in $C_1{-}x_{C_1}y_{C_1}z_{C_1}$
q_{1i}, q_{2i}, q_{3i}, θ_{1i}, θ_{2i}	The ith controlling parameters of each joint of the supporting robot
h	The wall thickness error
d	The setting wall thickness
x_{ti}, y_{ti}, z_{ti}, α_{ti}, β_{ti}	The parameters of the ith machining robot pose in $C_2{-}x_{C_2}y_{C_2}z_{C_2}$
q_{4i}, q_{5i}, q_{6i}, θ_{3i}, θ_{4i}	The ith controlling parameters of each joint of the machining robot
$\hat{q}_{1i}, \hat{q}_{2i}, \hat{q}_{3i}, \hat{\theta}_{1i}, \hat{\theta}_{2i}$	The ith actual parameters of each joint of the supporting robot
$\hat{q}_{4i}, \hat{q}_{5i}, \hat{q}_{6i}, \hat{\theta}_{3i}, \hat{\theta}_{4i}$	The ith actual parameters of each joint of the machining robot
$\hat{x}_{si}, \hat{y}_{si}, \hat{z}_{si}, \hat{\alpha}_{si}, \hat{\beta}_{si}$	The ith actual pose parameters of the supporting head in $C_1{-}x_{C_1}y_{C_1}z_{C_1}$
$\hat{x}_{ti}, \hat{y}_{ti}, \hat{z}_{ti}, \hat{\alpha}_{ti}, \hat{\beta}_{ti}$	The ith actual pose parameters of the cutter in $C_2{-}x_{C_2}y_{C_2}z_{C_2}$
d_r	The machining wall thickness
d_m	The actual measuring wall thickness by ultrasonic thickness gauge
L	The setting displacement from the steel ball of the end to supporting head
L_C	The actual displacement from the steel ball of the end to supporting head
$\lvert z_T\rvert$	The distance between the supporting head and the cutter in the axis direction

1 Introduction

Large thin-walled parts composed of aluminum alloys are widely used in aerospace industries such as for making aircraft skins and rocket tanks. The traditional machining method for large thin-walled parts is chemical milling which has the disadvantages of involving a complicated milling process, low machining accuracy, serious pollution generation, and low material utilization and machining efficiency, making it unable to satisfy the requirements desired for efficient machining and green manufacturing [1]. It is necessary to introduce auxiliary support to make a "tool-workpiece-fixture" machining system with sufficient rigidity due to the weak rigidity of large thin-walled parts in CNC milling. The traditional auxiliary molding support [2] uses a mold that is compatible with the shape of the workpiece to achieve the surface contact support of thin-walled parts, but the contact uniformity of the thin-walled parts and the mold is difficult to control. The molding support is only suitable for volume machining of the same shape because of its high cost and poor adaptability. In addition, a multi-point flexible auxiliary supporting method [2, 3] uses a retractable vacuum chuck unit and adapts the shape of the workpiece by arraying the supporting units; however, it is difficult to ensure the rigidity of the supporting unit interval. A mirror milling system was proposed by Dufieux [3] and Torres to achieve the green and efficient manufacturing of large thin-walled parts. The mirror milling system of Dufieux and Torres consists of a horizontal gantry milling machine, the gantry mirror supporting mechanism, and the auxiliary clamping mechanism. The gantry milling machine and gantry supporting mechanism with high-static stiffness, dynamic stiffness, absolute positioning accuracy, and repeatable positioning accuracy have good dynamic characteristics, but the gantry mechanism is large, poorly reconfigurable, and less flexible. In addition, conventional articulated industrial robots cannot easily replace traditional machine tools because of their weak rigidity and low positioning accuracy. On the other hand, the five-degree of freedom (DOF) hybrid robot with parallel mechanism has been widely used in machining and assembly [4] due to its large working space and high flexibility, stiffness, and precision. Compared with the traditional machining tools, the stiffness and positioning accuracy of the five-DOF hybrid robots are slightly low. But the requirements of light-loaded and small cut-depth machining for large thin-walled aluminous parts can be satisfied. Thus, a novel dual-robot mirror milling machining system is proposed by replacing the gantry milling machine and mirror support mechanism by dual five-DOF hybrid robots. The five-DOF hybrid supporting robot provides support and wall thickness measurement; the five-DOF hybrid machining robot is used for milling and error compensation. To ensure accurate equal remaining wall thickness, a collaborative machining method for dual-robot mirror milling is proposed.

Due to the cutting deformation and vibration, the accuracy of the remaining wall thickness is hard to guarantee. To suppress the deformation and vibration of large thin-walled parts during machining, an intelligent mirror

milling system based on dual supporting heads was presented [5]. The supporting track of the dual supporting head was established to ensure that at least one supporting head supports the parts during the machining process. It was verified experimentally that the deformation and chatter of the parts could be effectively reduced. The stiffness distribution of the thin-walled parts was studied [6], and equivalent stiffness models of the supporting mechanism and the stiffness model of the parts were established. The composite stiffness of the thin-walled parts with support was analyzed and optimized by adding redundant actuation. The relationship between the deformation and the vibrating amplitude of the parts around the machining position was studied [7, 8] to determine the optimal supporting position of the supporting head for the machining of equal wall thickness. The deformation and vibration suppression of thin-walled parts have been studied by the above researchers. However, these studies focus only on deformation and vibration suppression without paying attention to the machining wall thickness. Many scholars have performed substantial work to ensure the remaining wall thickness of large thin-walled parts. The deformation estimation models based on the cutting force were established [9, 10] to compensate the cutting deformation by planning and modifying the tool paths. Some deformation compensation strategies based on finite element method (FEM) was performed [11–14] to reduce the overtolerance of thin-walled parts. However, there are always some deviations between the theory model and the reality because of the complexity of milling dynamics. With the widespread application of touch-trigger probe, on-machine measurement (OMM) [15, 16] without bring in the refixturing positioning errors which are created by offline measurement is more frequently used to achieve error compensation by tool path compensation algorithm. To ensure the machining precision of large thin-walled parts, an online compensatory strategy and a control method for improved predictive compensation [17] were described in their proposed mirror milling system to reduce the cutting deformation and stochastic deformation during machining. In the strategy, an accurate predictive model of the parts was established for the real-time compensation of deformation by Kalman filtering, and the method can effectively compensate the time-lag problem and achieve good prediction accuracy. However, the machining accuracy depends on the accuracy of the model prediction and the deformation accuracy by laser displacement sensor, and the curved surface cannot be machined directly in the proposed mirror milling system [17] because its machining equipment is a three-axis machine tool. None of these methods compensate for the error by measuring the remaining wall thickness. A thickness measuring device [18] based on the principle of ultrasonic thickness was performed to measure the actual thickness of the thin-walled parts. However, the thickness measuring device requires an ultrasonic coupling agent and needs to offset during the machining so that the supporting head to provide effective support at the machining point for reducing deformation, and it is difficult to measure the wall thickness at the machining point. Therefore, a collaborative machining method is proposed to ensure the equal remaining wall thickness, and a contact thickness measurement for dual-robot geometric pose is performed in proposed method, which not only provides effective support at the machining point but also measures the real-time wall thickness and reduces the complexity of the system.

In this study, a novel mirror milling system for dual hybrid robots is proposed to machining the large thin-walled parts, and the collaborative machining method is described to guide the collaborative movement of robots in terms of the machining relationship. To achieve equal wall thickness machining, a contact thickness measurement method based on dual-robot geometric pose is performed to measure machining thickness, and the thickness errors are compensated by the machining hybrid robot in next interpolation period. The milling experiment finally proves the proposed collaborative machining method is effective for equal wall thickness machining. The remainder of this paper is organized as follows. The mirror milling system composition, the kinematics of hybrid robot, and the analysis of machining constraints are introduced in section 2. In section 3, the coordinate systems for the dual-robot collaborative machining are established and the collaborative machining method for thin-walled parts is presented in proposed mirror milling system. The machining wall thickness is obtained by the dual-robot endmost geometrical pose to guarantee machining accuracy. In section 4, the proposed method is validated through triangular grid machining experiment in proposed system. The following errors in joint space and task space are analyzed during the machining to further improve the accuracy of the wall thickness. The actual measuring wall thickness is obtained by ultrasonic thickness gauge to validate machining wall thickness. Finally, some conclusions and outlooks are summarized in section 5.

2 Mirror milling system and constraint analysis

2.1 The mirror milling system

The mirror milling system consists of the following components: machining robot, supporting robot, fixture, and control system, as shown in Fig. 1. The machining robot and supporting robot consist of an identical five-DOF

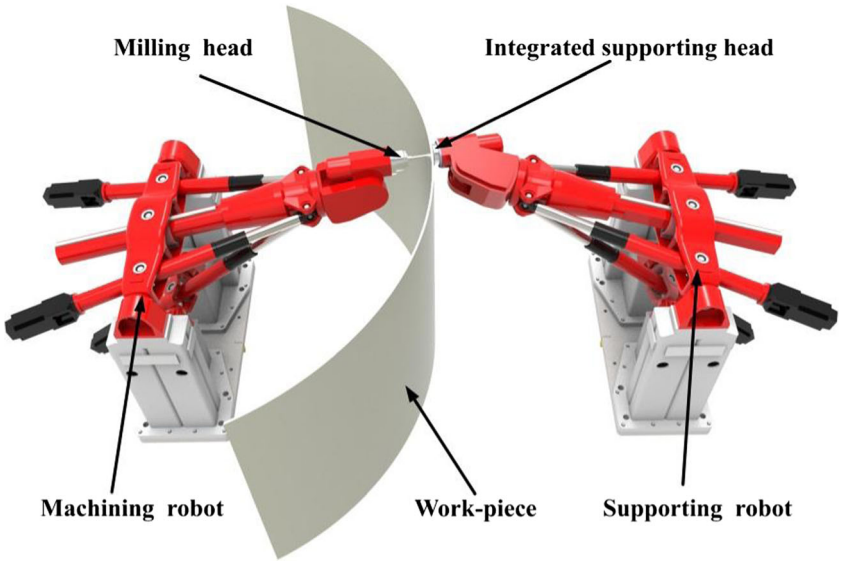

Fig. 1 Mirror milling system

hybrid mechanism—TriMule [19, 20]. The five-DOF hybrid robots are fixed on both sides of the workbench. The end effector of the machining robot is a milling cutter of the electric spindle-driven and is used for cutting machining and wall thickness error compensation. The end effector of the supporting robot is an integrated flexible supporting head. The structure for the 7-point supporting is used for the flexible supporting head, which consists of a central integrated supporting measuring cylinder [21] and six surrounding common cylinders. Steel balls 15 mm in diameter are fixed to the end of the flexible supporting head and provide the support. The flexible supporting head can reduce the deformation and vibration by improving the rigidity of the thin-walled parts in the direction of the cutter axis during the machining; the measured displacement of the center telescopic cylinder is fed back to the control system to calculate the machining wall thickness and ensure that the accuracy of wall thickness is satisfied.

2.2 Five-DOF hybrid mechanism

The body of the machining robot and supporting robot is composed of a five-DOF hybrid mechanism named TriMule. The mechanism is widely used because of its features, including a large workspace, being light weight, flexible movement, high stiffness, and low cost. The TriMule diagram is shown in Fig. 2.

TriMule consists of a three-DOF parallel mechanism part and a two-DOF series mechanism. The three-DOF parallel mechanism is connected by three UPS branches to the moving platform and the static platform; the two-DOF series mechanism is the AC pendulum, which is fixed on the moving platform. The following coordinate systems are established to explain the kinematic model of the TriMule mechanism, as shown in Fig. 2, including base coordinate system $B-xyz$, the coordinate system of the fixed moving platform $P-x_py_pz_p$, and the terminal coordinate system $C-x_cy_cz_c$. The orientation matrix $\mathbf{R}_p$ of the coordinate system $P-x_py_pz_p$ to the coordinate system $B-xyz$ is described by the rotation angle ψ about the x-axis and the rotation angle θ about the x_c-axis. The orientation matrix $\mathbf{R}_c$ of the coordinate system $C-x_cy_cz_c$ to the coordinate system $P-x_py_pz_p$ can be described by the rotation angle θ_1 about the $\mathbf{z}_p$-axis and the rotation angle θ_2 about the $\mathbf{X}_C$-axis. The orientation matrix $\mathbf{R}$ of the coordinate system $C-x_cy_cz_c$ to the coordinate system $B-xyz$ is obtained using the matrices $\mathbf{R}_c$ and $\mathbf{R}_p$.

$$\mathbf{R}_p = \mathrm{Rot}(x,\psi)\mathrm{Rot}\left(y_p,\theta\right) = [\boldsymbol{s}_1\ \boldsymbol{s}_2\ \boldsymbol{s}_3] \tag{1}$$

$$\mathbf{R}_c = \mathrm{Rot}\left(z_p,\theta_1\right)\mathrm{Rot}(x_c,\theta_2) \tag{2}$$

$$\mathbf{R} = \mathbf{R}_p\mathbf{R}_c = [\boldsymbol{u}\ \boldsymbol{v}\ \boldsymbol{w}] \tag{3}$$

where $\boldsymbol{s}_1$, $\boldsymbol{s}_2$, and $\boldsymbol{s}_3$ represent the three unit vectors of the coordinate system $P-x_py_pz_p$, and $\boldsymbol{u}$, $\boldsymbol{v}$, and $\boldsymbol{w}$ represent the three unit vectors of the coordinate system $C-x_cy_cz_c$.

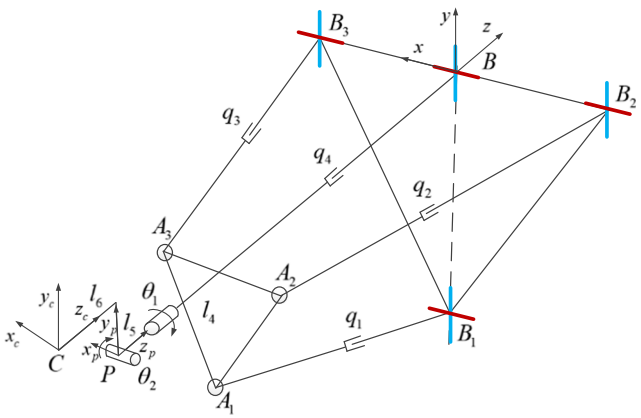

Fig. 2 The TriMule diagram

According to the closed-loop constraint equation, the position vector $\boldsymbol{r_p}$ of point P in the base coordinate system $B-xyz$ is given as

$$\boldsymbol{r_p} = \boldsymbol{b_i} + \boldsymbol{q_i}\ \boldsymbol{w_i} - \boldsymbol{a_i} \tag{4}$$

$$\boldsymbol{r_p} = -\boldsymbol{r_p}\ \boldsymbol{w_4} \tag{5}$$

where $i = 1, 2, 3$; $r_p = q_4 + l_4$; q_i represents the length of the rod in UPS branch i; $\boldsymbol{w_i}$ represents the unit vector of UPS branch i; $\boldsymbol{a_i} = \boldsymbol{R}\boldsymbol{a_{i0}}$; $\boldsymbol{a_{i0}} = (a_i \cos\gamma_i\ a_i \sin\gamma_i\ 0)^T$; and $\boldsymbol{b_i} = (b_i \cos\gamma_i\ b_i \sin\gamma_i\ 0)^T$

$$\gamma_i \begin{cases} -\pi/2, & i = 1 \\ 0, & i = 2 \\ \pi, & i = 3 \end{cases}$$

The length q_i and unit vector $\boldsymbol{w_i}$ of UPS branch i can be obtained by constructing the orientation matrix $\boldsymbol{R}_p$ and substituting Eq. (4).

$$q_i = \left|\boldsymbol{r_p} + \boldsymbol{a_i} - \boldsymbol{b_i}\right| \tag{6}$$

$$\boldsymbol{w_i} = \left(\boldsymbol{r_p} + \boldsymbol{a_i} - \boldsymbol{b_i}\right) / \boldsymbol{q_i} \tag{7}$$

The position vector $\boldsymbol{r_c}$ of point C in the base coordinate system $B-xyz$ is given as

$$\boldsymbol{r_c} = d_v \boldsymbol{v} + \boldsymbol{d_w}\ \boldsymbol{w} + \boldsymbol{r_p} \tag{8}$$

where $\boldsymbol{r_p}$ represents the position vector of point P, d_v and d_w represent the coordinates of $\boldsymbol{v}$ and $\boldsymbol{w}$ in $C-x_cy_cz_c$, respectively, and $\boldsymbol{w}$ represents the direction vector of the cutter axis by a rotation angle α about the x-axis and the rotation angle β about the y-axis from the initial direction.

θ_1 and θ_2 can be obtained from the constructed equation, which are not described in detail here.

The inverse kinematics of the TriMule mechanism uses the scale parameter and the pose (x, y, z, α, β) of the end actuator to solve for the lengths and angles $(q_1, q_2, q_3, \theta_1, \theta_2)$ of each branch. The forward kinematics can be obtained in an inverse manner.

2.3 The analysis of machining constraints

In the mirror milling process, the cutter and the supporting head are located on both sides of the thin-walled parts. The flexible supporting head at the end of the supporting robot is located normal to the supporting surface, maintained on the supporting surface along a predetermined off-line machining trajectory, and avoids the deformation of thin-walled parts due to "over-supporting." The surface of the parts is machined by the electric spindle-driven cutter of the machining robot, and the normal vectors of the cutter are always kept in the opposite direction from the vectors of the supporting head. The wall thickness of the parts is determined by the axial distance between the steel ball of the pneumatic flexible supporting end and the cutter of the machining robot. When the wall thickness error exceeds the tolerance, the cutter must first align to an orientation collinear with the normal direction of the supporting head and then feed along the collinear direction to compensate error.

In the machining process for parts with continuous equal wall thickness, the pose of the cutter and supporting head changes with the surface of the thin-walled parts, but the collaborative relationship between the supporting head and cutter needs to be always satisfied. Thus, the collaborative relationship, including that between two end-effect actuators of five-DOF hybrid robots and the collaborative relationship of the two five-DOF hybrid robots, is obtained.

3 The collaborative machining method

3.1 Definition of coordinate system

To more clearly express the relationship of the pose between the cutter of the machining robot and the supporting head of the supporting robot in mirror milling and establish the collaborative equation for the machining robot and supporting robot, the following coordinate systems are defined. As shown in Fig. 3, $B_1{-}x_{B_1}y_{B_1}z_{B_1}$ represents the base coordinate system of the supporting robot, and the origin of the coordinate system is built in the center of the supporting robot turning bracket; $C_1{-}x_{C_1}y_{C_1}z_{C_1}$ represents the tool coordinate system of the supporting robot, where the origin is located at the center of the supporting head at the zero pose of the supporting robot. $S-x_Sy_Sz_S$ represents the followed coordinate system of the supporting head, which fixes the end of the supporting head and changes with the pose of the supporting head. The origin coincides with the center of the supporting head. At the zero pose of the supporting robot, the followed coordinate system of the supporting head $S-x_Sy_Sz_S$ is completely coincident with the tool coordinate system of the supporting robot, and the normal vector of the supporting head is the reversed z_S-axis direction of the followed coordinate system on the supporting head. $C_y{-}x_{C_y}y_{C_y}z_{C_y}$ means the supporting cylinder coordinate system, and the origin, is located at the center of the steel ball at the end of the integrated supporting measuring cylinder.

Similar to the supporting robot, the base coordinate system $B_2{-}x_{B_2}y_{B_2}z_{B_2}$ and tool coordinate system $C_2{-}x_{C_2}y_{C_2}z_{C_2}$ of the machining robot are established. $T-x_Ty_Tz_T$ represents the followed coordinate system of the cutter, which fixes the end of the cutter and changes with the pose of the cutter. The origin coincides with the center of the cutter. In the zero pose of the machining robot, the followed coordinate system of the cutter $T-x_Ty_Tz_T$ is completely coincident with the tool coordinate system of the machining robot, and the normal vector of the cutter is the reversed z_T-axis direction of the cutter followed

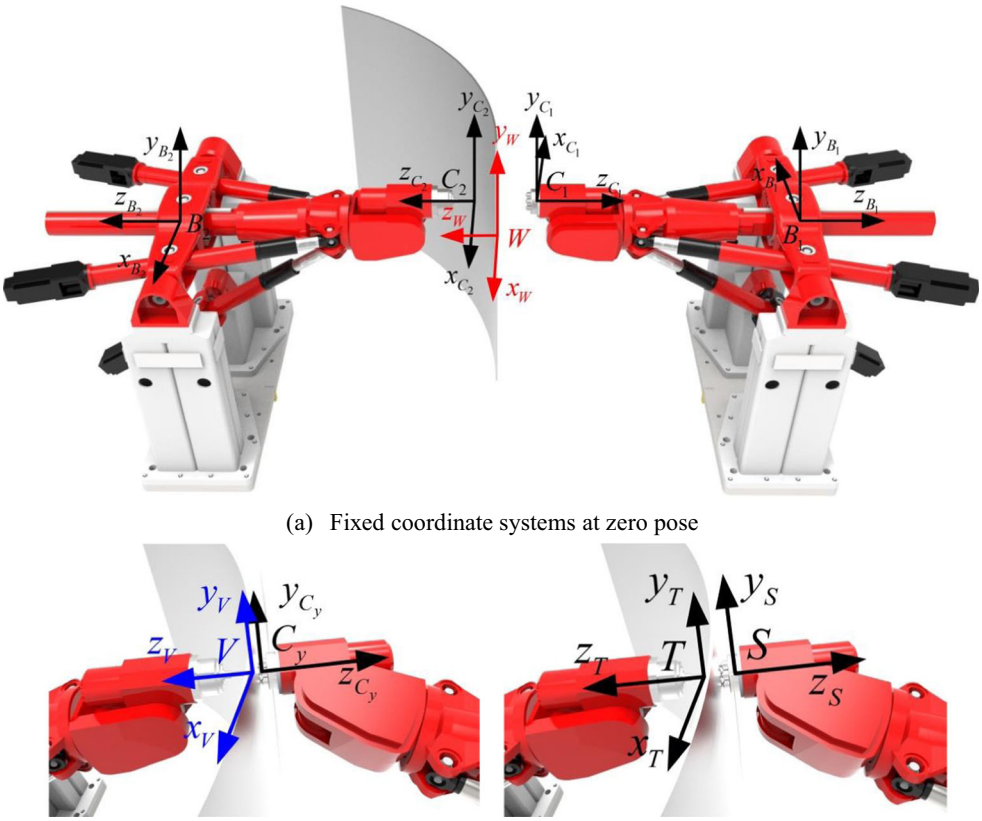

Fig. 3 Coordinate systems. **a** Fixed coordinate systems at zero pose. **b** Motion coordinate system during machining

coordinate system. $V-x_Vy_Vz_V$ represents the virtual coordinate system of the cutter, and the coordinate origin is located at the center of the cutter head under an ideal wall thickness. The coordinate origin of the workpiece coordinate system $W-x_Wy_Wz_W$ is located on the supporting surface of the thin-walled parts and can adjust the specific position according to the processing need.

3.2 Coordinated machining for equal wall thickness

According to the collaborative relationship between the supporting robot and the machining robot during machining, the coordinated machining equation of the dual robots is derived as follow:

$$ {}^{B_2}\mathbf{T}_{C_2}\cdot{}^{C_2}\mathbf{T}_T\cdot{}^{T}\mathbf{T}_V = {}^{B_2}\mathbf{T}_{B_1}\cdot{}^{B_1}\mathbf{T}_{C_1}\cdot{}^{C_1}\mathbf{T}_W\cdot{}^{W}\mathbf{T}_{C_y}\cdot{}^{C_y}\mathbf{T}_V \tag{9} $$

$$ {}^{C_1}\mathbf{T}_W\cdot{}^{W}\mathbf{T}_{C_y} = {}^{C_1}\mathbf{T}_S\cdot{}^{S}\mathbf{T}_{C_y} \tag{10} $$

In the above formula, ${}^{B_2}\mathbf{T}_{C_2}$ represents the homogeneous transformation matrix from the tool coordinate system of the machining robot C_2–$x_{C_2}y_{C_2}z_{C_2}$ to the base coordinate system of the machining robot B_2–$x_{B_2}y_{B_2}z_{B_2}$. ${}^{B_2}\mathbf{T}_{B_1}$ represents the homogeneous transformation matrix from the base coordinate system of the supporting robot B_1–$x_{B_1}y_{B_1}z_{B_1}$ to the base coordinate system of the machining robot B_2–$x_{B_2}y_{B_2}z_{B_2}$. ${}^{B1}\mathbf{T}_{C_1}$ represents the homogeneous transformation matrix from the tool coordinate system of the supporting robot C_1–$x_{C_1}y_{C_1}z_{C_1}$ to the base coordinate system of the supporting robot B_1–$x_{B_1}y_{B_1}z_{B_1}$. ${}^{C_1}\mathbf{T}_W$ represents the homogeneous transformation matrix from the workpiece coordinate system $W-x_Wy_Wz_W$ to the tool coordinate system of the supporting robot C_1–$x_{C_1}y_{C_1}z_{C_1}$. ${}^{C_2}\mathbf{T}_T$ represents the homogeneous transformation matrix from the cutter followed coordinate system $T-x_Ty_Tz_T$ to the tool coordinate system of the machining robot C_2–$x_{C_2}y_{C_2}z_{C_2}$. ${}^{T}\mathbf{T}_V$ represents the homogeneous transformation matrix from the virtual cutter coordinate system $V-x_Vy_Vz_V$ to the cutter followed coordinate system $T-x_Ty_Tz_T$. ${}^{W}\mathbf{T}_{C_y}$ represents the homogeneous transformation matrix from the supporting cylinder coordinate system C_y–$x_{C_y}y_{C_y}z_{C_y}$ to the workpiece coordinate system $W-x_Wy_Wz_W$. ${}^{C_y}\mathbf{T}_V$ represents the homogeneous transformation matrix from the virtual cutter coordinate system $V-x_Vy_Vz_V$ to the supporting cylinder coordinate system C_y–$x_{C_y}y_{C_y}z_{C_y}$. ${}^{C_1}\mathbf{T}_S$ represents the homogeneous transformation matrix from the followed coordinate system $S-x_Sy_Sz_S$ of supporting head to the tool coordinate system of the supporting robot C_1–$x_{C_1}y_{C_1}z_{C_1}$. ${}^{S}\mathbf{T}_{C_y}$ represents the homogeneous transformation matrix from the supporting cylinder coordinate system C_y–$x_{C_y}y_{C_y}z_{C_y}$ to the followed coordinate system $S-x_Sy_Sz_S$ of supporting head.

As shown in Fig. 4, the main steps of the equal wall thickness machining strategy for the mirror milling system are as follows:

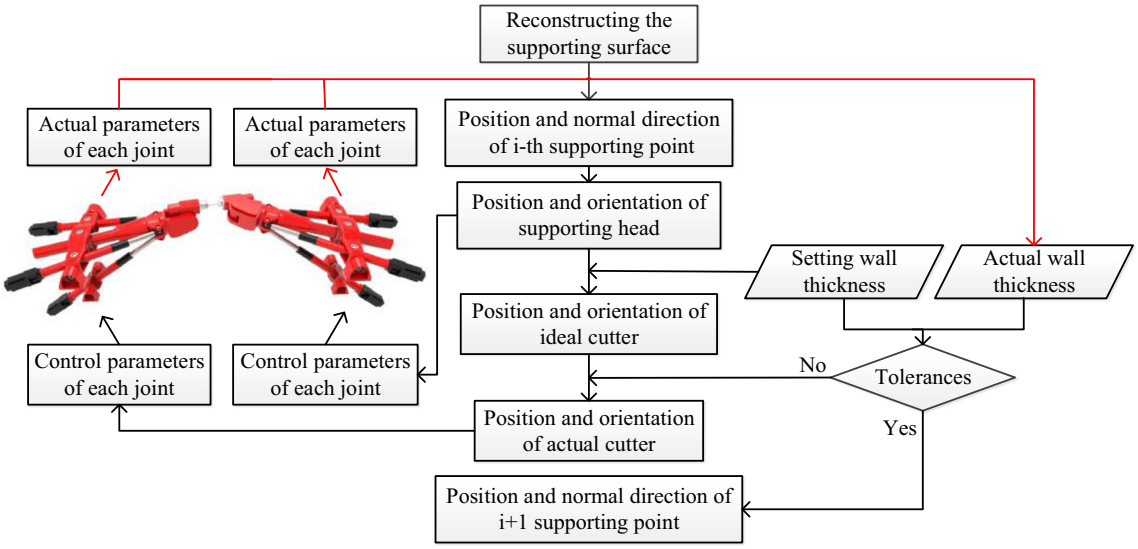

Fig. 4 Machining strategy

(I) After the thin-walled parts are clamped, the supporting surface of the thin-walled parts is scanned [22] by a laser to obtain the position parameters of the supporting surface in the workpiece coordinate system $W-x_W y_W z_W$. The parameters of the supporting surface are reconstructed to obtain the mathematical model of the thin-walled parts. According to the reconstruction model, off-line trajectory of supporting robot was planned. The normal vector direction of each point on the supporting surface of the thin-walled parts is determined by the rotation angles α and β, which represent the angles at which the initial orientation of the supporting head rotates sequentially around the x_W and y_W axes of the workpiece coordinate system to the normal vector direction of the position (x, y, z).

(II) When the ith supporting position (x_i, y_i, z_i) of off-line trajectory of the supporting robot is arrived, the rotation angles α_i and β_i at this pose are determined according to the reconstructed mathematical model of the supporting surface and off-line trajectory. The homogeneous transformation matrix ${}^{W}\mathbf{T}_{C_y}$ from the supporting cylinder coordinate system to the workpiece coordinate system is obtained through the parameters $(x_i, y_i, z_i, \alpha_i, \beta_i)$.

$$
{}^{W}\mathbf{T}_{C_y} = \begin{bmatrix} \cos\beta_i & \sin\beta_i\sin\alpha_i & \sin\beta_i\cos\alpha_i & x_i \\ 0 & \cos\alpha_i & -\sin\alpha_i & y_i \\ -\sin\beta_i & \cos\beta_i\sin\alpha_i & \cos\beta_i\cos\alpha_i & z_i \\ 0 & 0 & 0 & 1 \end{bmatrix} \times \begin{bmatrix} -1 & 0 & 0 & 0 \\ 0 & 1 & 0 & 0 \\ 0 & 0 & -1 & 0 \\ 0 & 0 & 0 & 1 \end{bmatrix} \tag{11}
$$

According to the setting displacement of the integrated supporting and measuring cylinder, the displacement L between the steel ball of the end and the origin of the supporting head followed coordinate system is determined, and homogeneous transformation matrix ${}^{S}\mathbf{T}_{C_y}$ is obtained. The homogeneous transformation matrix ${}^{C_1}\mathbf{T}_S$ from the followed coordinate system of supporting head to the tool coordinate system of the supporting robot is derived using Eq. (10).

$$
{}^{C_1}\mathbf{T}_S = {}^{C_1}\mathbf{T}_W \cdot {}^{W}\mathbf{T}_{C_y} \cdot \left[{}^{S}\mathbf{T}_{C_y}\right]^{-1} \tag{12}
$$

$$
{}^{C_1}\mathbf{T}_S = \begin{bmatrix} n_x & s_x & a_x & x_{si} \\ n_y & s_y & a_y & y_{si} \\ n_z & s_z & a_z & z_{si} \\ 0 & 0 & 0 & 1 \end{bmatrix} \tag{13}
$$

The ith supporting position (x_{si}, y_{si}, z_{si}) in the tool coordinate system of the supporting robot is obtained by the homogeneous matrix ${}^{C_1}\mathbf{T}_S$. The rotation angles α_{si} and β_{si} are determined by Eqs. (14)–(16).

$$
\phi = a\tan2\left(n_y, n_x\right) \tag{14}
$$

$$
\alpha_{si} = a\tan2\left(\sin\phi \cdot a_x - \cos\phi \cdot a_y, -\sin\phi \cdot s_x + \cos\phi \cdot s_y\right) \tag{15}
$$

$$
\beta_{si} = a\tan2\left(-n_z, \cos\phi \cdot n_x + \sin\phi \cdot n_y\right) \tag{16}
$$

The control parameters $(q_{1i}, q_{2i}, q_{3i}, \theta_{1i}, \theta_{2i})$ of each joint of the supporting robot are solved in the ith supporting position through the inverse kinematics model of the supporting robot and the pose parameters.

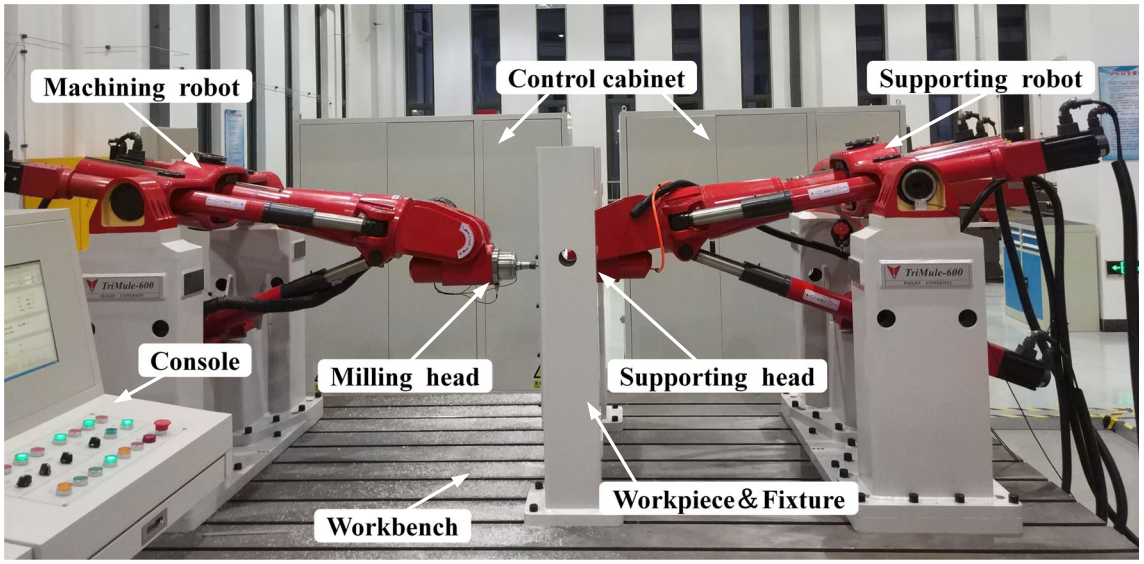

Fig. 5 Mirror milling system of dual robots

(III) The homogeneous matrix ${}^{C_2}\mathbf{T}_T$ from the cutter followed coordinate system to the tool coordinate system of the machining robot is obtained by Eq. (9).

$$ {}^{C_2}\mathbf{T}_T = \left[{}^{B_2}\mathbf{T}_{C_2}\right]^{-1}\cdot{}^{B_2}\mathbf{T}_{B_1}\cdot{}^{B_1}\mathbf{T}_{C_1}\cdot{}^{C_1}\mathbf{T}_W\cdot\mathbf{T}WC_y\cdot{}^{C_y}\mathbf{T}_V\cdot\left[{}^{T}\mathbf{T}_V\right]^{-1} \tag{17} $$

where

$$ {}^{T}\mathbf{T}_V = \begin{bmatrix} 1 & 0 & 0 & 0 \\ 0 & 1 & 0 & 0 \\ 0 & 0 & 1 & -h \\ 0 & 0 & 0 & 1 \end{bmatrix} \quad {}^{C_y}\mathbf{T}_V = \begin{bmatrix} -1 & 0 & 0 & 0 \\ 0 & 1 & 0 & 0 \\ 0 & 0 & -1 & -d \\ 0 & 0 & 0 & 1 \end{bmatrix} $$

The wall thickness error h in the position transfer vector $(0, 0, -h)^T$ of the homogeneous matrix ${}^{T}\mathbf{T}_V$ is calculated by comparing between the machining thicknesses and setting thickness in the following; the parameter d of the homogeneous matrix ${}^{C_y}\mathbf{T}_V$ represents the setting machining wall thickness.

According to Eqs. (13)–(16) in step I, the ith pose parameters $(x_{ti}, y_{ti}, z_{ti}, \alpha_{ti}, \beta_{ti})$ of the cutter are obtained. The controlling parameters $(q_{4i}, q_{5i}, q_{6i}, \theta_{3i}, \theta_{4i})$ of each joint on the machining robot are solved in the ith machining position through the inverse kinematics model of the machining robot and the pose parameters of the cutter.

(IV) The actual parameters $\left(\hat{q}_{1i}, \hat{q}_{2i}, \hat{q}_{3i}, \hat{\theta}_{1i}, \hat{\theta}_{2i}\right)$ of each joint of the supporting robot and the actual parameters $\left(\hat{q}_{4i}, \hat{q}_{5i}, \hat{q}_{6i}, \hat{\theta}_{3i}, \hat{\theta}_{4i}\right)$ of each joint of the machining robot are obtained by the motor encoder. According to the kinematics forward solution model of the supporting robot and the machining robot, the actual pose parameters $\left(\hat{x}_{si}, \hat{y}_{si}, \hat{z}_{si}, \hat{a}_{si}, \hat{\beta}_{si}\right)$ of the supporting head are obtained in the tool coordinate system of the supporting robot C_1–$x_{C_1}y_{C_1}z_{C_1}$, and the actual pose parameters $\left(\hat{x}_{ti}, \hat{y}_{ti}, \hat{z}_{ti}, \hat{\alpha}_{ti}, \hat{\beta}_{ti}\right)$ of the cutter are obtained in the tool coordinate system of the machining robot C_2–$x_{C_2}y_{C_2}z_{C_2}$. Next, the homogeneous transformation matrices ${}^{C1}\hat{\boldsymbol{T}}_S$ and ${}^{C2}\hat{\boldsymbol{T}}_T$ can be determined. The homogeneous matrix ${}^{S}\hat{\boldsymbol{T}}_T$ is then obtained by Eqs. (9) and (10).

$$ {}^{S}\hat{\boldsymbol{T}}_T = \left[{}^{C1}\hat{\boldsymbol{T}}_S\right]^{-1}\cdot\left[{}^{B_1}\mathbf{T}_{C_1}\right]^{-1}\cdot\left[{}^{B_2}\mathbf{T}_{B_1}\right]^{-1}\cdot{}^{B_2}\mathbf{T}_{C_2}\cdot{}^{C2}\hat{\boldsymbol{T}}_T \tag{18} $$

The position components (x_T, y_T, z_T) can be obtained by the homogeneous matrix ${}^{S}\hat{\boldsymbol{T}}_T$. The parameter $|z_T|$ indicates the displacement between the supporting head and the

Table 1 The machining parameters

Parameters	Description
Dimension	Equilateral triangle with 232-mm sides
Material	Aluminum alloy 6061
Spindle speed	5000 rpm
Feed rates	2000 mm/min
Setting thickness	4.000 mm
Depth of cut	0.5 mm
Cutter diameter	16 mm
Number of flutes	3

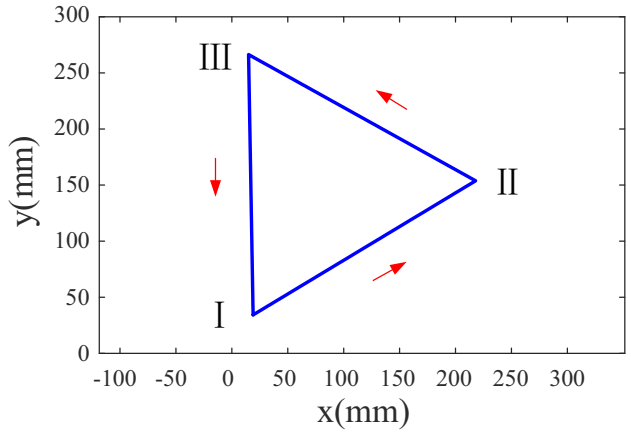

Fig. 6 Thin-walled triangular grid

cutter in the axis direction. The machining wall thickness d_r is obtained by Eq. (19):

$$d_r = |z_T| - L_C \tag{19}$$

$$h = d_r - d \tag{20}$$

The actual displacement L_C between the steel ball of the end and the origin of the supporting head followed coordinate system can be measured using the integrated supporting measuring cylinder. The wall thickness error h is calculated using Eq. (20). If the tolerance of the machining wall thickness is not met, the wall thickness error h is substituted into step III and compensated by the machining robot in next interpolation period; otherwise, the $(i+1)$th position will be machined by repeating steps (II–IV).

4 Test verification

Before the machining experiment, the simulation analysis of the curved surface and the flat plate was performed to ensure equal wall thicknesses. The results showed that the proposed method is consistent for the curved surface and flat plate. The rectangular plate was used to verify the effectiveness of the proposed method in the mirror milling system due to the limitation of experimental conditions. The proposed mirror milling system is described in this study as shown in Fig. 5. The mirror milling system consists of the machining robot, supporting robot, clamp, spindle, flexible supporting head, worktable, control cabinet, operating table, etc. Panasonic Minas A6 series servo motors and drivers are used for each driving joint of the machining robot and supporting robot. The PMAC is used to control the drivers and communicate with the host computer. The 7.5-kW air-cooled spindle is fixed at the end of the machining robot, and the integrated flexible supporting head is fixed at the end of the supporting robot. The raw material for the machining is a 1000-mm × 800-mm rectangular piece and the wall thickness is 8 mm. The material is aluminum alloy 6061.

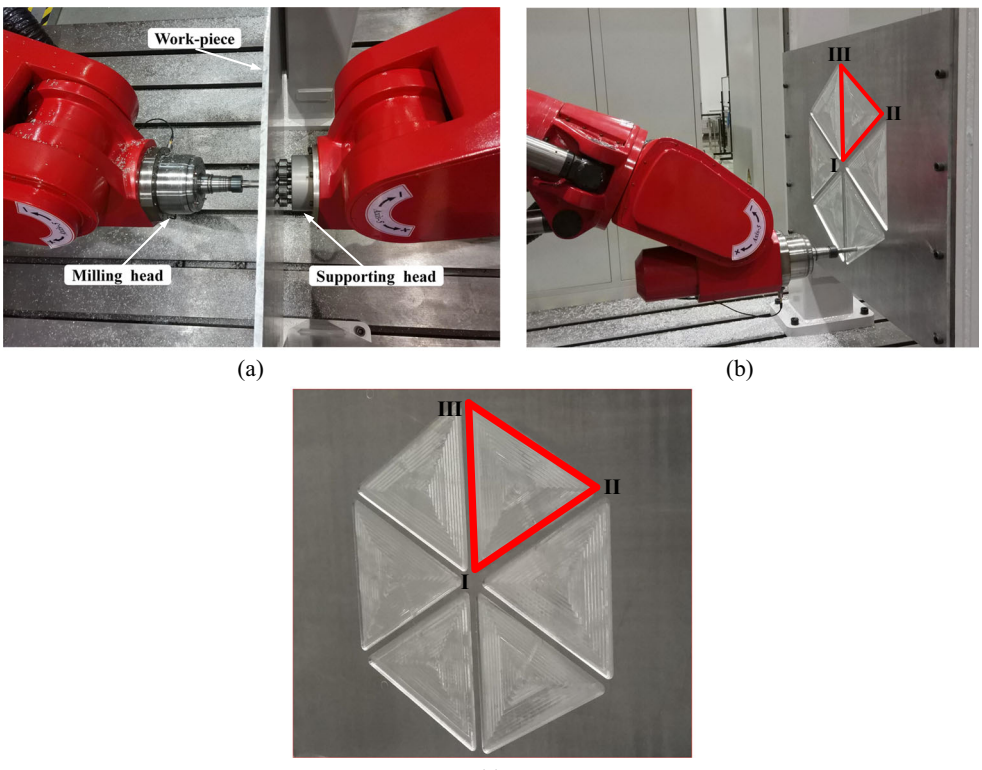

Fig. 7 Machining of thin-walled triangular grids

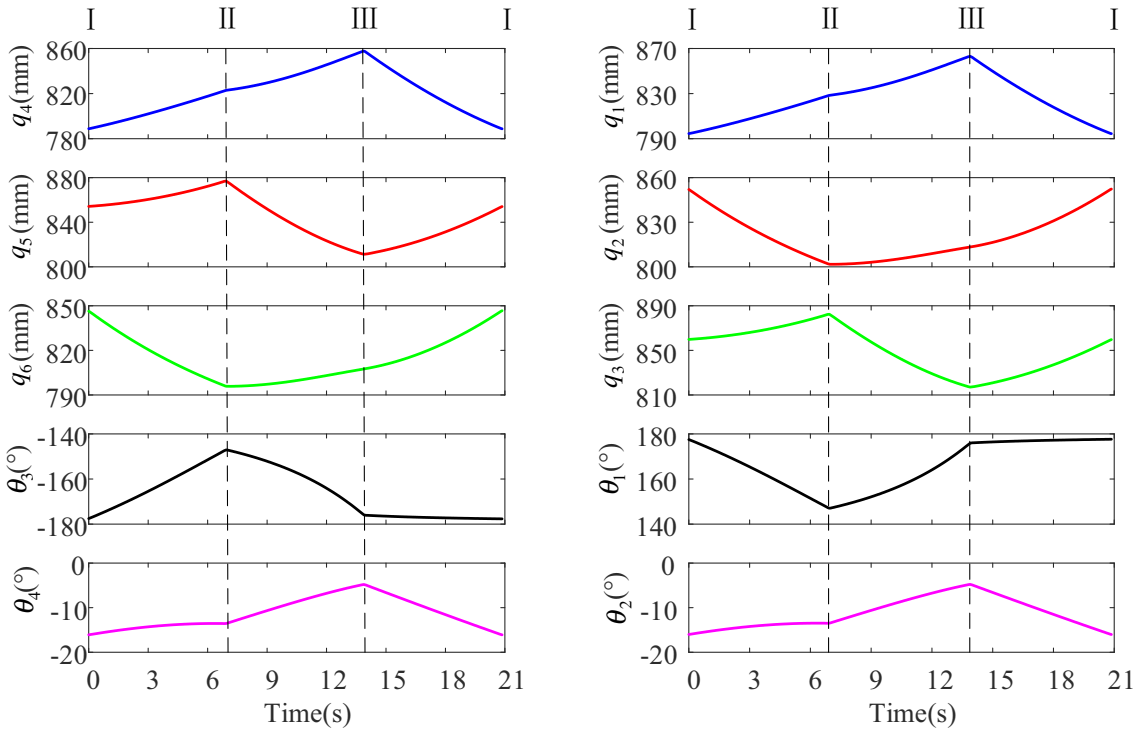

Fig. 8 Position control parameters of joint motor

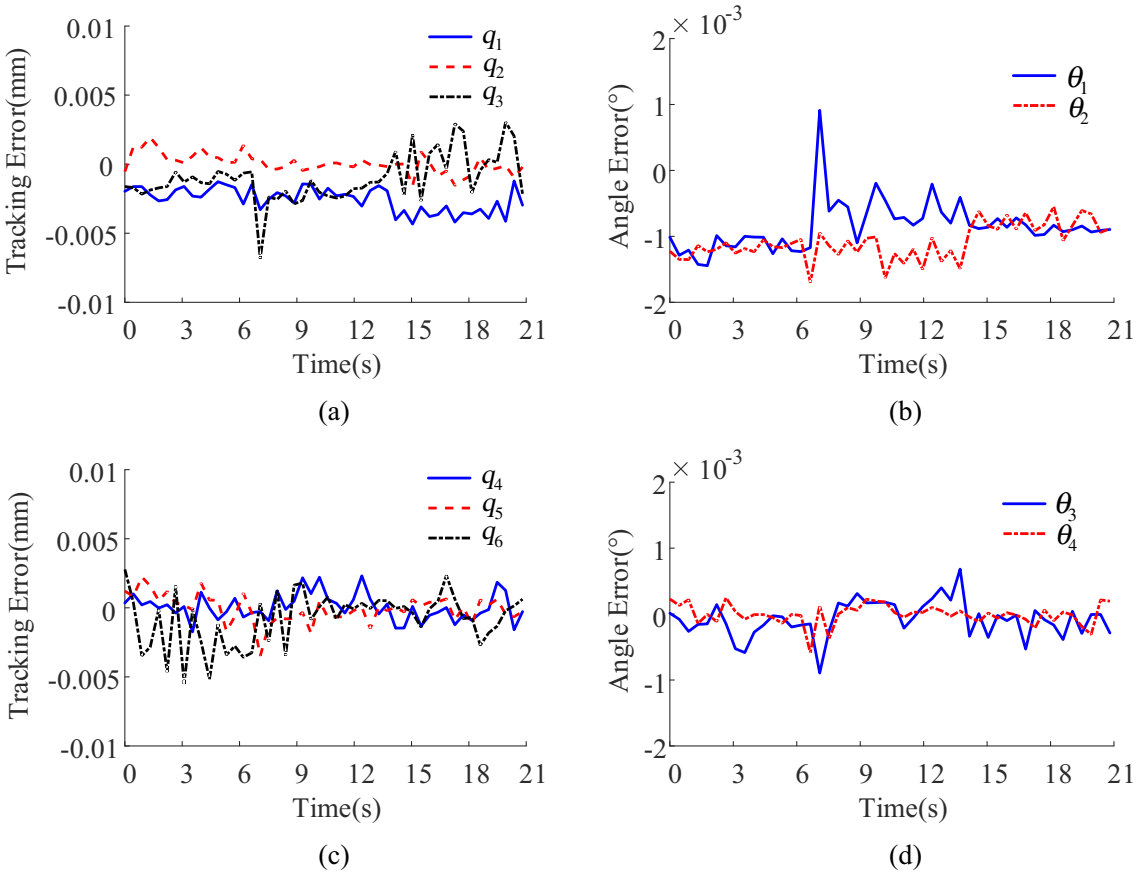

Fig. 9 Motion errors of the driving joint

To prove the effectiveness of the proposed method, the thin-walled triangular aerospace grids are milled to validate the effectiveness in the dual-robot mirror milling system. The analysis of the last layer's contour machining is conducted on the triangular grids. The machining parameters of the thin-walled triangular grids are shown in Table 1. The processing time is determined by the machining parameters of the feed rate and the depth of cut, and the feed rate and depth of cut depend on the processing craftwork. In the same processing craftwork, the processing efficiency and processing time of proposed milling system are comparable with other mirror milling systems. In addition, the servo system cycle is 0.442 ms and the interpolation period is five servo cycles in proposed system. Linear arc interpolation is adopted in the processing. The tolerance of the machining wall thickness is ± 0.05 mm to control wall thickness.

To reduce the deformation of the thin-walled parts, the machining begins in the middle of the thin-walled triangle and proceeds from inside to outside. The machining trajectory of the triangular grid contour in the workpiece coordinate system is shown in Fig. 6, and the order of machining is I → II → III → I.

The machining of the thin-walled triangular grids is shown in Fig. 7a, b. The finished grids are shown in Fig. 7c.

According to the machining parameters, the position control parameters of each joint motor during the I → II → III → I contouring process are obtained, as shown in Fig. 8.

The position control parameters of each joint motor are compared with the actual position parameters, and the following errors of the machining robot and supporting robot in the joint space can be obtained, as shown in Fig. 9. From Fig. 9a, b, the following error amplitudes of the triad branches of the supporting robot are all less than 0.007 mm, and the following error amplitudes of the AC swing angles are all less than 0.002°; the following error amplitudes of the triad branches of the machining robot are all less than 0.005 mm, and the following error amplitudes of the AC swing angles are all less than 0.001°. Various interesting phenomena can be noted from Fig. 9. In the vicinity of $t = 7$ s (around position II), there is a large mutation of following errors in translational joint q_3 and rotational joint θ_1 of the supporting robot. There is a small change in following errors in moving joints q_5 and q_6 of the machining robot. There are obvious following errors in the rotation of joints θ_3 and θ_4 of the machining robot. In the vicinity of $t = 14$ s (around position III), there is a large fluctuation in the following error of moving joint q_3 and a small stepping amplitude in the following error step of rotating joint θ_2 with the supporting robot. There is a certain mutation in the

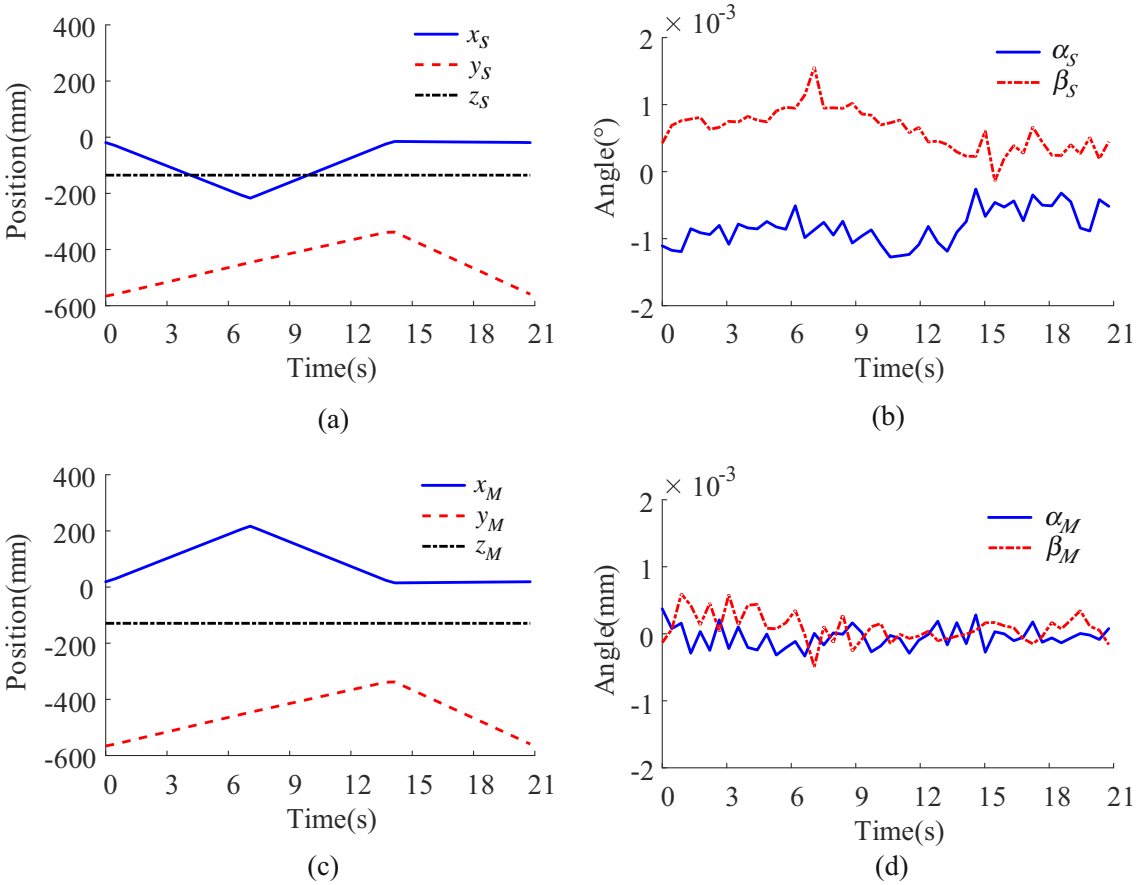

Fig. 10 Task space position and orientation

rotating joint θ_3 of the machining robot. Combined with the position control parameters of the joint motor in Fig. 8, the possible cause of the mutation in the following error at $t = 7$ s and $t = 14$ s is the change in the joint reversing friction force.

To better measure the collaborative performance of the dual robots, the actual position of each joint of the supporting robot and the machining robot is substituted into the forward kinematics model, and the terminal poses of the supporting robot and the machining robot in the task space are obtained. The pose of the supporting robot in its tool coordinate system is shown in Fig. 10a, b; the pose of the machining robot in its tool coordinate system is shown in Fig. 10c, d.

The following errors during the mirror milling process in the task space of the supporting robot are shown in Fig. 11a, b; the following errors in the task space of the machining robot are shown in Fig. 11c, d. As shown in Fig. 11, the following errors of the position in the task space are less than 0.03 mm, and the following errors of the rotation angle are less than 0.002°. The following performance is poor along the x- and y-axis, and the following performance is better along the z-axis for the machining robot and supporting robot. One possible reason for this is that z-axis is the thickness direction of the workpiece, and the feed in the z-axis direction is smaller for machining of pieces of equal wall thickness; the machining plane is located in the xy-plane, and the cutting motion is along the x- and y-directions. In addition, it can be noted that the pose following errors of the supporting robot are larger from Fig. 11b. Thus, the necessity of the pneumatic flexible supporting head is proved.

As shown in Fig. 12a, the real-time displacement L_C between the end of the steel ball and the followed coordinate system of the supporting head is determined by the displacement sensor of the integrated supporting measuring cylinder. The homogeneous transformation matrices ${}^{C2}\hat{\boldsymbol{T}}_T$ and ${}^{C1}\hat{\boldsymbol{T}}_S$ can be determined by the actual pose parameters of the cutter and the supporting head. The homogeneous matrix ${}^{S}\hat{\boldsymbol{T}}_T$ is obtained by Eq. (18). $|z_T|$ indicates the displacement between the supporting head and the cutter in the axis direction, and can be determined by the position components of ${}^{S}\hat{\boldsymbol{T}}_T$. The machining wall thickness d_r is indirectly obtained by Eq. (19). The machining wall thickness d_r and the setting wall thickness d are shown in Fig. 12c. Furthermore, the actual measuring wall thickness d_m is obtained by ultrasonic thickness gauge to validate machining wall thickness in Fig. 12b and the results are shown in Fig. 12c. The actual measuring wall thickness error is less than ± 0.2 mm from Fig. 12c. It can be noticed that the machining wall thickness and the actual measuring wall

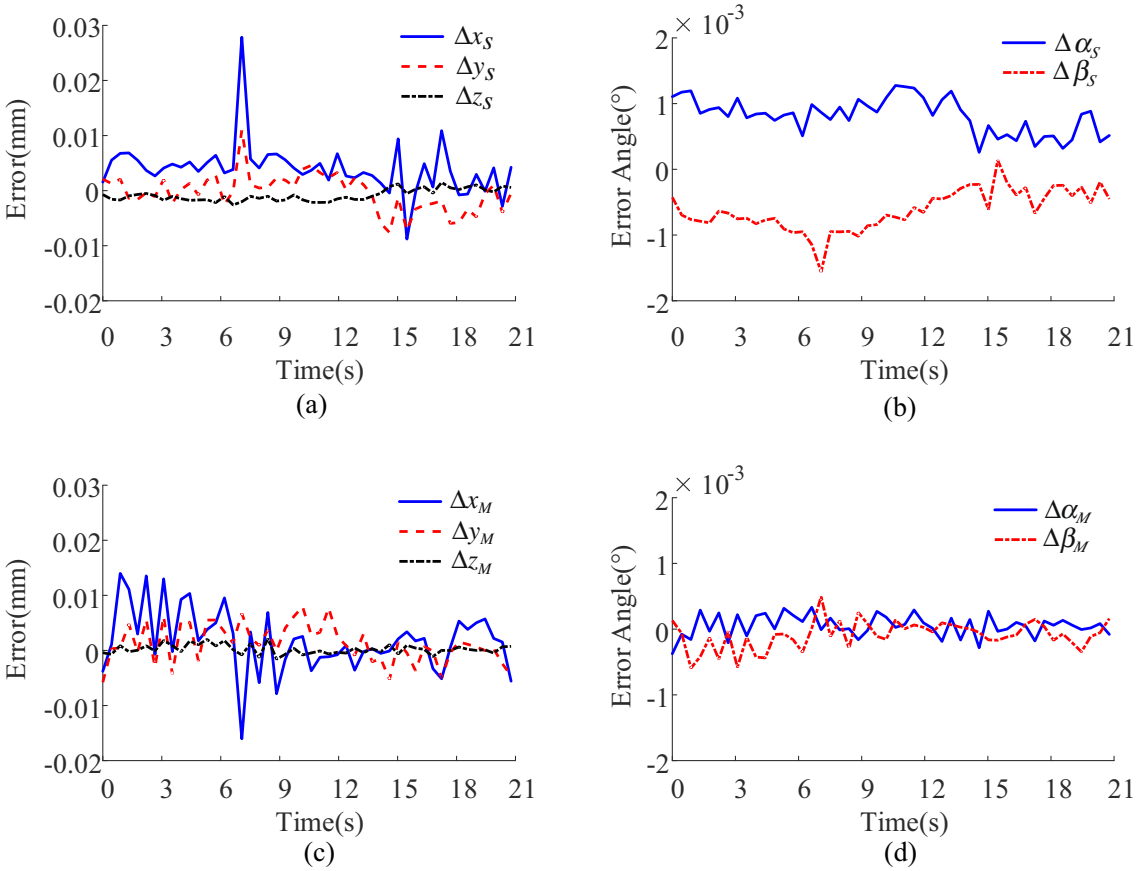

Fig. 11 Motion errors of task space

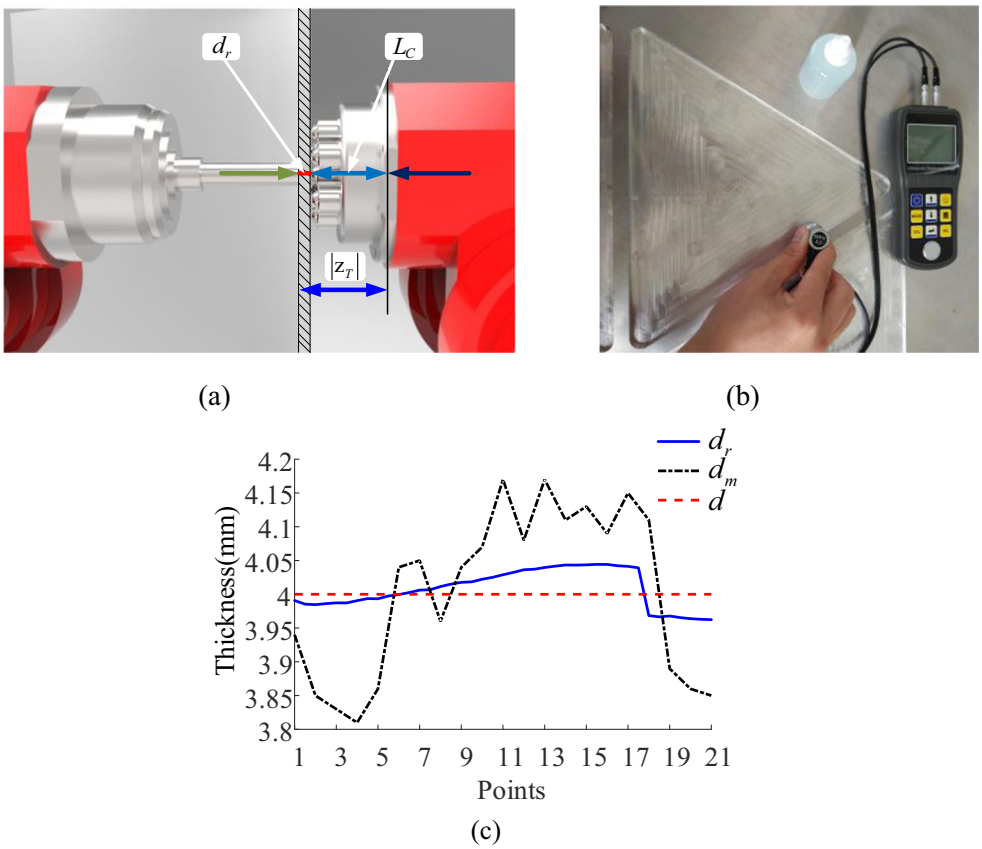

Fig. 12 Actual wall thickness

thickness have the same trend. The effectiveness of the proposed method for the mirror milling system can thus be validated.

5 Conclusion

For the mirror milling of large thin-walled parts, a dual-robot collaborative machining method for equal wall thickness is proposed in this study. The pose of the cutter and the flexible supporting head can be determined through the proposed method. To improve processing accuracy of the remaining wall thickness, a contact thickness measurement for dual-robot geometric pose is performed by the flexible supporting head integrated displacement sensor to obtain the real-time wall thickness in proposed method, and the wall thickness errors are compensated by the machining robot. The integrated supporting head provides effective support at machining position and suppresses the milling deformation and vibration during the machining. A large thin-walled triangular grid has been used to validate the effectiveness of the proposed method. The experimental results show that the proposed method can be used to effectively perform machining tasks with the dual-robot mirror milling system. The position following errors of the supporting head and the cutter are less than 0.03 mm in the task space; the orientation following errors of the supporting head and the cutter are less than 0.002°. The machining wall thickness is indirectly determined by the dual-robot endmost geometrical pose, and the machining wall thickness error is less than ± 0.05 mm. The actual wall thickness is measured by ultrasonic thickness gauge and the actual wall thickness errors are less than ± 0.2 mm. In the next research, a grating-based robotic full-closed loop control will be implemented to improve control accuracy and the control algorithm of the hybrid robot will be further studied to improve the actual wall thickness machining accuracy. In addition, the proposed method is also suitable for other similar systems and provides practical references.

Funding information The authors gratefully acknowledge the support of the National Basic Research Program of China (Grant No.2014CB046603) and the National Natural Science Foundation of China (Grant No.91648202).

References

1. Zhang T (2011) Up-to-date technology for precision machining of aircraft skin thickness-greenhouse machining technology for the CNC milling instead of chemical milling. Trainer 4:25–29

2. Zhou K (2012) Flexible tooling and fixture technology of large thin-wall part manufacturing for aircraft. Aeronaut Manuf Technol 3:34–39
3. Zhang Z, Xu X (2010) MMS: the latest green skin machining system. Aeronaut Manuf Technol 19:84–86. https://doi.org/10.3969/j.issn.1671-833X.2010.19.011
4. Uriarte L, Zatarain M, Axinte D, Yagüe-Fabra J, Ihlenfeldt S, Eguia J, Olarra A (2013) Machine tools for large parts. CIRP Ann-Manuf Technol 62:731–750. https://doi.org/10.1016/j.cirp.2013.05.009
5. Lan J, Lin B, Huang T, Xiao J, Zhang X, Fei J (2016) Path planning for support heads in mirror-milling machining system. Int J Adv Manuf Technol (in press) 91(1–4):1–12. https://doi.org/10.1007/s00170-016-9725-7
6. Hao J, Zhao Y, Wang H, Sheng D (2015) Synthetical stiffness analysis and optimization of mirror support mechanism for thin-walled structures. Mach Des Res 31(2):155–159 163
7. Bao Y, Zhu X, Kang R, Dong Z, Zhang B, Guo D (2016) Optimization of support location in mirror-milling of aircraft skins. Proc Inst Mech Eng B J Eng Manuf:1–8. https://doi.org/10.1177/0954405416673110
8. Bao Y, Dong Z, Kang R, Li Z, Yuan Y (2016) Milling force and machining deformation in mirror milling of aircraft skin. Adv Mater Res 1136:149–155. https://doi.org/10.4028/www.scientific.net/AMR.1136.149
9. Gao Y, Ma J, Jia Z, Wang F, Si L, Song D (2016) Tool path planning and machining deformation compensation in high-speed milling for difficult-to-machine material thin-walled parts with curved surface. Int J Adv Manuf Technol 84(9):1757–1767. https://doi.org/10.1007/s00170-015-7825-4
10. Wan M, Zhang W, Qin G, Wang Z (2008) Strategies for error prediction and error control in peripheral milling of thin-walled workpiece. Int J Mach Tools Manuf 48(12):1366–1374. https://doi.org/10.1016/j.ijmachtools.2008.05.005
11. He N, Wang Z, Jiang C, Zhang B (2003) Finite element method analysis and control stratagem for machining deformation of thin-walled components. J Mater Process Technol 139(1–3):332–336. https://doi.org/10.1016/S0924-0136(03)00550-8
12. Dong Z, Jiao L, Wang X, Liang Z, Liu Z, Yi J (2016) FEA-based prediction of machined surface errors for dynamic fixture workpiece system during milling process. Int J Adv Manuf Technol 85(1):299–315. https://doi.org/10.1007/s00170-015-7854-z
13. Rai J, Xirouchakis P (2008) FEM-based prediction of workpiece transient temperature distribution and deformations during milling. Int J Adv Manuf Technol 42(5):429–449. https://doi.org/10.1007/s00170-008-1610-6
14. Ratchev S, Liu S, Becker A (2005) Error compensation strategy in milling flexible thin-wall parts. J Mater Process Technol 162:673–681. https://doi.org/10.1016/j.jmatprotec.2005.02.192
15. Guiassa R, Mayer J, St-Jacques P, Engin S (2015) Calibration of the cutting process and compensation of the compliance error by using on-machine probing. Int J Adv Manuf Technol 78(5):1043–1051. https://doi.org/10.1007/s00170-014-6714-6
16. Huang N, Bi Q, Wang Y, Sun C (2014) 5-axis adaptive flank milling of flexible thin-walled parts based on the on-machine measurement. Int J Mach Tools Manuf 84:1–8. https://doi.org/10.1016/j.ijmachtools.2014.04.004
17. Wang X, Bi Q, Zhu L, Ding H (2016) Improved forecasting compensatory control to guarantee the remaining wall thickness for pocket milling of a large thin-walled part. Int J Adv Manuf Technol 94:1–12. https://doi.org/10.1007/s00170-016-9785-8
18. Zhang K, Zhang L, Zhang J (2015) A adaptive compensation processing method of aeronautical aluminum alloy thin walled work piece. International Journal of Research in Engineering and Science10: 52–56
19. Dong C, Liu H, Liu Q, Huang T, Chetwynd D (2018) An approach for type synthesis of overconstrained 1T2R parallel mechanisms. Computational Kinematics. Springer, Cham, pp 274–281. https://doi.org/10.1007/978-3-319-60867-9_31
20. Huang T, Dong C, Liu H, Qin X, Mei J, Liu Q, Wang M. A novel 5-DOF hybrid robot with multi-axes gimbal holder, China Patent, CN201510401279.9, 2015.10.21
21. Xiao J, Xu F, Zhao S, Huang T, Lin B (2017) An integrated pneumatic rigid mirror milling flexible support device for real-time measurement of thickness, China Patent. CN201710251630X 07:14
22. Liu H, Wang Y, Jia Z, Guo D (2015) Integration strategy of on-machine measurement (OMM) and numerical control (NC) machining for the large thin-walled parts with surface correlative constraint. Int J Adv Manuf Technol 80(9):1721–1731. https://doi.org/10.1007/s00170-015-7046-x